Revisiting the Austral Spring Extratropical Southern Hemisphere zonally asymmetric circulation using complex Empirical Orthogonal Functions

Elio Campitelli · Leandro B. Díaz ·
Carolina Vera ·

Abstract abstract

Elio Campitelli
Universidad de Buenos Aires, Facultad de Ciencias Exactas y Naturales, Departamento de
Ciencias de la Atmósfera y los Océanos. Buenos Aires, Argentina.
CONICET – Universidad de Buenos Aires. Centro de Investigaciones del Mar y la Atmósfera
(CIMA). Buenos Aires, Argentina.
CNRS – IRD – CONICET – UBA. Instituto Franco-Argentino para el Estudio del Clima y
sus Impactos (IRL 3351 IFAECI). Buenos Aires, Argentina.
E-mail: elio.campitelli@cima.fcen.uba.ar

Leandro B. Díaz
Universidad de Buenos Aires, Facultad de Ciencias Exactas y Naturales, Departamento de
Ciencias de la Atmósfera y los Océanos. Buenos Aires, Argentina. CONICET – Universidad
de Buenos Aires. Centro de Investigaciones del Mar y la Atmósfera (CIMA). Buenos Aires,
Argentina. CNRS – IRD – CONICET – UBA. Instituto Franco-Argentino para el Estudio
del Clima y sus Impactos (IRL 3351 IFAECI). Buenos Aires, Argentina.

Carolina Vera
Universidad de Buenos Aires, Facultad de Ciencias Exactas y Naturales, Departamento de
Ciencias de la Atmósfera y los Océanos. Buenos Aires, Argentina. CONICET – Universidad
de Buenos Aires. Centro de Investigaciones del Mar y la Atmósfera (CIMA). Buenos Aires,
Argentina. CNRS – IRD – CONICET – UBA. Instituto Franco-Argentino para el Estudio
del Clima y sus Impactos (IRL 3351 IFAECI). Buenos Aires, Argentina.

1 Introduction

The large-scale extratropical circulation in the Southern Hemisphere (SH) is strongly zonally symmetric, but its zonal departures are highly relevant for regional impacts (e.g. Hoskins and Hodges 2005). They strongly modulate weather systems and regional climate through promoting longitudinally different latitudinal transport of heat, humidity, and momentum (K. E. Trenberth 1980; M. N. Raphael 2007) and could even be related to the occurrence of high-impact climate extremes (Pezza, Rashid, and Simmonds 2012).

Zonally asymmetric circulation is typically described by the amplitude and phase of zonal waves obtained by Fourier decomposition of geopotential heights or sea-level pressures at each latitude (e.g. van Loon and Jenne 1972; K. E. Trenberth 1980; Turner et al. 2017). This approach suggests that zonal waves 1 and 3 explain almost 99% of the total variance in the annual mean 500-hPa pattern at 50ºS (van Loon and Jenne 1972). K. F. Trenberth and Mo (1985) concluded that wave 3 plays a role in the development of blocking events. In addition, previous works have identified at extratropical and subpolar latitudes, wave-like patterns with dominant wavenumbers 3-4, also exerting distinctive regional impacts. M. N. Raphael (2007) shows that variability in the planetary wave 3 projected onto its climatological location is associated with anomalies in the Antarctic sea-ice concentration.

The Fourier decomposition relies on the assumption that the circulation can be meaningfully described in terms of zonal waves of constant amplitude along a latitude circle. However, this is not valid for meridionally propagating waves or zonal waves with localised amplitudes. Addressing this limitation, the Fourier technique can be generalized to integrate all planetary wave amplitude regardless of wave number, by computing the wave envelope (Irving and Simmonds 2015). The latter makes possible to represent planetary waves with different amplitude at different longitudes, but it removes all information about phase and wave number. With this approach, Irving and Simmonds (2015) showed that planetary wave amplitude in general is associated to Antarctic sea-ice concentration and temperature, as well as to precipitation anomalies in regions of significant topography in SH mid-latitudes and Antarctica.

Another extensively used approach to characterize the SH tropospheric circulation anomalies, is by computing Empirical Orthogonal Functions (EOF, also known as Principal Component Analysis). Within the EOF framework, the Southern Annular Mode (SAM) appears as the leading mode of variability of the SH circulation (Fogt and Marshall 2020). SAM represents a relatively zonally symmetric pattern of alternating low pressures in polar latitude and a ring of high pressures in high latitudes with an embedded wave 3 pattern that is more prominent in the Pacific sector. The 2nd and 3rd EOFs, usually known as Pacific–South American Patterns (PSA) 1 and PSA2 patterns, respectively, describe meridionally propagating wave trains that originate in the eastern equatorial Pacific and Australian-Indian Ocean sector, and travel towards the South Atlantic following a great-circle arch along the Antarctic coast (Mo and Paegle 2001). These patterns influence precipitation anomalies

in South America (Mo and Paegle 2001). Although these patterns are usually derived by applying EOF to temporal anomalies, (M. Raphael 2003) also applied EOF methods specifically to zonal anomalies. More recently, (Irving and Simmonds 2016) proposed a novel methodology for objectively identifying the PSA pattern using Fourier decomposition.

Patterns resulting from EOF analyses are more flexible than Fourier decomposition derived modes in the sense that they can capture oscillation patterns that cannot be characterised by purely sinusoidal waves with constant amplitude. Nonetheless, they are restricted to standing oscillation modes and could not represent properly propagating or phase-varying features such as zonal waves. A single EOF can also represent a mixture of two or more physical modes.

A third methodology commonly used consists on identifying particular features of interest and creating indices using simple methods such as averages and differences. Examples of this methodology are the SAM Index of (Gong and Wang 1999), the SH wave 3 activity index defined by M. N. Raphael (2004) and the SH zonally asymmetric circulation index from Hobbs and Raphael (2010). These derived methods are grounded on other methods such as Fourier decomposition or EOF to identify the centres of action for the described phenomena and can be useful to characterise features that are not readily apparent with these methods. It is commonly easy the computation of these kind of indices, but they could be unable to capture non-stationary patterns.

An alternative methodology that has been proposed to study travelling and standing waves is complex Empirical Orthogonal Functions (Horel 1984). This method extends EOF analysis to capture oscillations with varying amplitude and phase and has been applied to the time domain on water level to study tide-river interactions (Laurel-Castillo and Valle-Levinson 2020) and temperature and precipitation anomalies (e.g. Krokhin and Luxemburg 2007; Gelbrecht, Boers, and Jürgen Kurths 2018). To our knowledge, complex EOF has not been applied in the spatial domain to capture the phase-varying nature of planetary waves.

Some of the zonally asymmetric patterns of the SH circulation variability described previously, appear to have experienced secular changes. For instance, M. Raphael (2003) found that the amplitude of the zonal wave 1 experienced a large increase and that the zonal wave 3 experienced changes in its annual cycle between 1958 and 1996. However, little is known yet about variability and trends of these patterns.

The general goal of this study is to improve the description and understanding of the zonally asymmetric extratropical SH circulation using complex Empirical Orthogonal Functions, which allow to describe phase varying planetary waves with variable amplitudes along a latitude circle. In addition, it is proposed to expand the knowledge of the simultaneous behaviour of SH asymmetric circulation in the troposphere and the stratosphere.

We restrict this paper to the September-October-November (SON) trimester. We chose this season because it showed the strongest and more clearly inter-

pretable results in a preliminary analysis of the four season. This is is consistent with previous research that shows that this season experiences a maximum in tropical teleconnections (Cazes-Boezio, Robertson, and Mechoso 2003) and stratosphere-troposphere interactions (Lim, Hendon, and Thompson 2018).

In Section 2 we describe the methods. In Section 3.1, we analyse the spatial patterns of each complex EOF. In Section 3.2 we study the spatial regressions with geopotential height and temperature anomalies. In Section 3.3, we analyse the relationship between cEOF1 and Ozone, and between cEOF2 with the SAM and the PSA. In Section 3.4 we study tropical forcings that explain the variability of each cEOF. Finally, in Section 3.5 we show the relationship between these modes of variability and precipitation anomalies in South America and Oceania.

2 Data and Methods

`methods`

2.1 Data

`data`

We used monthly geopotential height, air temperature, ozone mixing ratio, and total ozone column (TOC) at 2.5° longitude by 2.5° latitude of horizontal resolution and 37 vertical isobaric levels from the European Centre for Medium-Range Weather Forecasts Reanalysis version 5 [ERA; Hersbach et al. (2019)] for the period 1979-2019. Most of our analysis is restricted to the post-satellite era to avoid any confounding factors arising from the incorporation of satellite observations, but we also used the preliminary back extension of ERA5 from 1950 to 1978 (Bell et al. 2020) to describe long-term trends. We derived streamfunction at 200 hPa from ERA5 vorticity using the FORTRAN subroutine FISHPACK (Adams, Swartztrauber, and Sweet 1999) and we computed horizontal wave activity fluxes following Plumb (1985). Sea Surface Temperature (SST) monthly fields are from Extended Reconstructed Sea Surface Temperature (ERSST) v5 (Huang et al. 2017) and precipitation monthly data from the CPC Merged Analysis of Precipitation (P. Xie and Arkin 1997), with a 2.5° resolution in latitude and longitude. The rainfall gridded dataset is based on information from different sources such as rain gauge observations, satellite inferred estimations and the NCEP-NCAR reanalysis, and it is available since 1979 to present.

2.2 Methods

`methods-1`

The study is restricted to the spring season, defined as the September-October-November (SON) trimester. We compute seasonal means for the different variables, averaging monthly values weighted by the number of days in each month. We use 200 hPa level to represent the high troposphere and 50 hPa to represent the lower stratosphere.

The amplitude of the zonal waves was obtained through the Fourier transform of the spatial field at each latitude circle. For the analysis of wave 1,

we computed its amplitude and phase by averaging (area-weighted) the data for each variable and each SON between 75°S and 45°S, and then extracting the wave-1 component of the Fourier spectrum. We chose this latitude band because it is wide enough to capture most of the relevant anomalies of SH mid-latitudes.

We computed the level-dependent SAM index as the leading EOF of year-round monthly geopotential height anomalies south of 20ºS at each level for the whole period according (Baldwin and Thompson 2009). We further split the SAM into its zonally symmetric and zonally asymmetric components (S-SAM and A-SAM indices respectively). These indices were obtained by projecting the zonally asymmetric and zonally symmetric part of the SAM spatial pattern onto monthly geopotential height fields, as proposed by Campitelli, Díaz, and Vera (2022). Seasonal indices of the Pacific South American patterns (PSA1 and PSA2) were calculated – in agreement with Mo and Paegle (2001) – as the third and fourth leading EOF of seasonal mean anomalies for SH 500 hPa geopotential height.

Linear trends were computed by Ordinary Least Squares (OLS) and the 95% confidence interval was computed assuming a t-distribution with the appropriate residual degrees of freedom (D. Wilks 2011).

2.3 Complex Empirical Orthogonal Functions (cEOF)

`complex-empirical-orthogonal-functions-ceof`

In standard way of applying EOF analysis zonal waves may appear as pairs of EOFs, that could be degenerated representing similar patterns but shifted in phase (Horel 1984). Figure 1 shows the four eading EOFs of SON geopotential height zonal anomalies at 50 hPa south of 20°S. It is clear that the first two EOFs represent the same zonal wave 1 pattern and the last two represent a same zonal wave pattern with shorter wavenumber and four centers of action shifted by 1/4 wavelength. A similar EOF structure can be seen in 200 hPa (not shown). Since each pair of EOFs seem to represent the same phase-varying structure, it would be desirable to combine them into a single index with amplitude and phase.

ON the other hand, complex Empirical Orthogonal Functions (cEOF) is a useful method to characterise zonal waves, associated with phase-varying structures (Horel 1984). This method involves computing EOF on the analytic representation of the original field. That representation is a complex field in which the real part is the original data and the imaginary part is the original data shifted by 90°at each spectral frequency – i.e. its Hilbert transform. The Hilbert transform is usually understood in terms of time-varying signal. However, in this work we apply the Hilbert transform at each latitude circle and at each considered time. Since each latitude circle is a periodic domain, this procedure does not suffer from edge effects.

The result of the cEOF methodology is a set of complex spatial patterns and complex time series. The real and imaginary part of each spatial pattern represent the two phases of wave-like spatial patterns that are in quadrature.

EOF1   EOF2

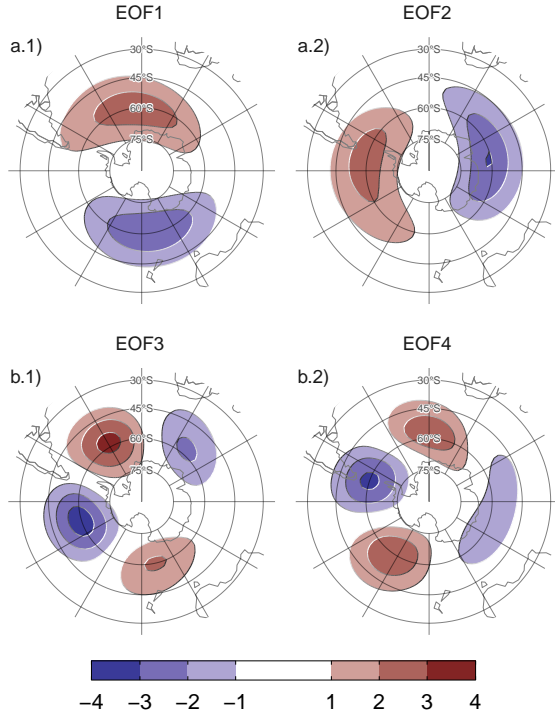EOF3   EOF4

Fig. 1: Spatial patterns of the four leading EOFs of SON zonal anomalies of geopotential height at 50 hPa south of 20°S for the 1979 – 2019 period (arbitrary units).

Table 1: Coefficient of determination (R^2) between the absolute magnitude of complex EOFs computed separately at 200 hPa and 50 hPa (p-values lower than 0.01 in bold).

200 hPa	50 hPa		
	cEOF1	cEOF2	cEOF3
cEOF1	**0.29**	0.01	0.03
cEOF2	0.00	**0.59**	0.02
cEOF3	0.00	0.00	0.01

The magnitude and argument of each complex time series represent the amplitude and phase of each zonal wave.

The cEOF methodology is applied to SON geopotential height zonal anomalies south of 20°S separately at 50 and 200 hPa. Table 1 shows the coefficient of determination between time series of the amplitude of each cEOF across levels. There is a high degree of correlation between the magnitude of the respective cEOF1 and cEOF2 at each level. The spatial patterns of the 50 hPa and 200 hPa cEOFs are also similar (not shown).

Both the spatial pattern similarity and the high temporal correlation of cOEFs computed at 50 hPa and 200 hPa suggest that these are, to a large extent, modes of joint variability. This motivates the decision of performing complex EOF jointly between levels. Therefore cEOFs were computed using data from both levels at the same time. In that sense each cEOF has a spatial component that depends on longitude, latitude and level, and a temporal component that depends only on time.

The phase of principal components is defined up to an additive constant. For real principal components, this constant can be either 0 or π, corresponding to a change in sign. For complex principal components, it can be any number between 0 and 2π (Horel 1984). Since any choice is arbitrary and equally valid, we chose the phase of each cEOF so that the real and imaginary parts are aligned with meaningful phases in our analysis. This procedure does not create a spurious correlation, it only takes a known relationship and aligns it with a specific phase. For the first complex principal component, the phase was chosen so that the time series corresponding to the real part has the maximum correlation with the zonal wave 1 of Total Ozone Column between 75°S and 45°S. This also nearly minimises the correlation with the imaginary part. For the second complex principal component, the phase was chosen so that the coefficient of determination between the Oceanic Niño Index (Bamston, Chelliah, and Goldenberg 1997) and the real part was minimized, which also nearly maximizes the correlation with the imaginary part.

While we compute these complex principal components using data from 1979 to 2019, we extended the complex time series back to the $1950 - 1978$ period by projecting monthly geopotential height zonal anomalies standardised by level south of 20ºS onto the corresponding spatial patterns.

We performed linear regressions to quantify the association between the cEOFs and other variables (e.g. geopotential height, temperature, precipitation, and others). For each cEOF, we computed regression maps by fitting a multiple linear model involving both the real and the imaginary part. To obtain the linear coefficients of a variable X with the imaginary and real parts of each cEOF we fit the equation

$$X(\lambda, \phi, t) = \alpha(\lambda, \phi) \operatorname{Im}(\text{cEOF}) + \beta(\lambda, \phi) \operatorname{Re}(\text{cEOF}) + X_0(\lambda, \phi) + \epsilon(\lambda, \phi, t)$$

where λ and ϕ are the longitude and latitude, t is the time, α and β are the linear regression coefficients for imaginary and real parts respectively, X_0 and ϵ are the constant and error terms respectively.

We evaluated statistical significance using a two-sided t-test and, in the case of regression maps, p-values were adjusted by controlling for the False Discovery Rate (Benjamini and Hochberg 1995; D. S. Wilks 2016) to avoid misleading results from the high number of regressions (Walker 1914; Katz and Brown 1991).
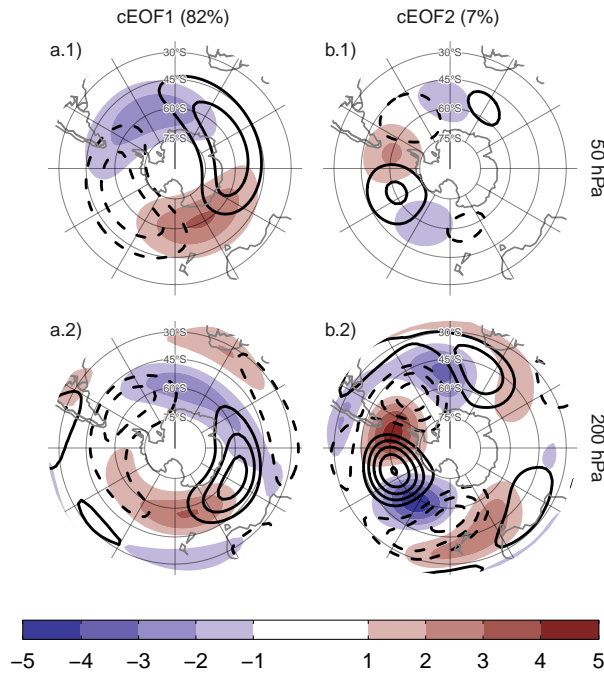
cEOF1 (82%)   cEOF2 (7%)

Fig. 2: Spatial patterns for the two leading cEOFs of SON zonal anomalies of geopotential height at 50 hPa and 200 hPa for the 1979 – 2019 period. The shading (contours) corresponds to real (imaginary) part. Arbitrary units.

2.4 Computation procedures

computation-procedures

We performed all analysis in this paper using the R programming language (R Core Team 2020), using data.table (Dowle and Srinivasan 2020) and metR (Campitelli 2020) packages. All graphics are made using ggplot2 (Wickham 2009). We downloaded data from reanalysis using the ecmwfr package (Hufkens 2020) and indices of the ENSO with the rsoi package (Albers and Campitelli 2020). The paper was rendered using knitr and rmarkdown (Y. Xie 2015; Allaire et al. 2020).

3 Results

results

3.1 cEOF spatial patterns

spatial

To describe the variability of the circulation zonal anomalies, the spatial and temporal parts of the first two leading cEOFs of zonal anomalies of geopotential height at 50 hPa and 200 hPa, computed jointly at both levels, are shown in Figures 2 and 3. The first mode (cEOF1) explains 82% of the variance, while the second mode (cEOF2) explains a smaller fraction (7%). In the spatial
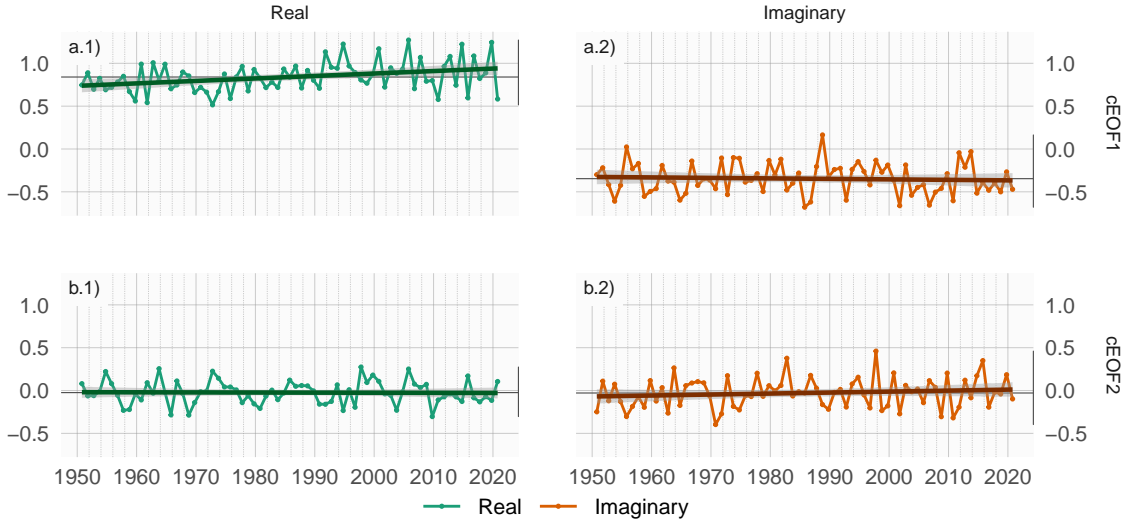
Fig. 3: Time series extended using ERA5 back extended preliminary edition (period 1950 – 1978) and ERA5 (period 1979 – 2019). Dark straight line is the linear trend. Black horizontal and vertical line mark the mean value and range of each time series, respectively.

`fig:extended-series`

²⁴⁸ patterns (Fig. 2), the real and the imaginary components are in quadrature
²⁴⁹ by construction, so that each cEOF describe a single wave-like pattern whose
²⁵⁰ amplitude and position (i.e. phase) is controlled by the magnitude and phase
²⁵¹ of the temporal cEOF. The wave patterns described by these cEOFs match
²⁵² the patterns seen in the traditional EOFs of Figure 1.

²⁵³   The cEOF1 (Fig. 2 column a) is a hemispheric wave 1 pattern with maxi-
²⁵⁴ mum amplitude at high latitudes. At 50 hPa the Real cEOF1 has the maximum
²⁵⁵ of the wave 1 at 150ºE and at 200 hPa, the maximum is located at around
²⁵⁶ 175ºE indicating a westerly shift in phase. The cEOF2 (Fig. 1 column b) shows
²⁵⁷ also a zonal wave-like structure with maximum amplitude at high latitudes,
²⁵⁸ but with shorter spatial scales. In particular, the dominant structure at both
²⁵⁹ levels is a wave 3 but with larger amplitude in the pacific sector. This modu-
²⁶⁰ lated amplitude is especially apparent at 200 hPa. There is no apparent phase
²⁶¹ shift but the amplitude of the pattern is greatly reduced in the stratosphere,
²⁶² suggesting that this barotropic mode represents mainly tropospheric variabil-
²⁶³ ity.

²⁶⁴   All cEOFs have non zero mean (Fig. 3) because the geopotential fields that
²⁶⁵ enter into the cEOFs algorithm are anomalies with respect to the zonal mean
²⁶⁶ instead of the time mean. However, cEOF2's mean is almost zero, which indi-
²⁶⁷ cates that only cEOF1 includes variability that significantly projects onto the
²⁶⁸ mean zonally anomalous field. There is no significant simultaneous correlation
²⁶⁹ between the time series. Both cEOFs show year-to-year variability but show
²⁷⁰ no evidence of decadal variability.

A significant upward trend in the real component of cEOF1 is evident (Fig. 3a.1, p-value = 0.0037) while there is no significant trend in any of the complex components of cEOF2. The positive trend in the Real cEOF1 translates into a positive trend in cEOF1 magnitude, but not in the phase (not shown). This long-term change indicates an increase in the magnitude of the high latitude zonal wave 1. In agreement, M. Raphael (2003) detected a step change after around 1975 in the temporal evolution of leading EOF computed from August-September-October 500 hPa zonal geopotential height anomalies, which is similar to the cEOF1.

3.2 cEOFs Regressions

regressions

In the previous section, cEOFs were applied to zonal anomalies, that is anomalies derived by removing the zonally mean values in order to isolate the main characteristics of the main zonal waves characterizing the circulation in the SH. In this section, regression fields were computed using the full fields of the variables in order to describe the influence of the cEOFs on the temporal anomalies.

Figure 4 shows regression maps of SON geopotential height anomalies upon cEOF1. At 50 hPa (Figure 4 row a), both the Real and Imaginary cEOF1 are associated with planetary wave 1 patterns, that are 90º out of phase. Their phases coincide with the ones shown in Figure 2a.1, with the positive centre of the Real cEOF1 located towards the dateline, and the one of the Imaginary cEOF1 located over East Antarctica. Instead of a wave-1 pattern, regressed anomalies describe a monopole with its centre displaced from the South Pole. The latter indicates an influence of cEOF1 in modulating the polar vortex.

The regression maps for cEOF1 at 200 hPa (Figure 4 row b) are similarly influenced by the zonally symmetric circulation. It is only possible to partially distinguish the wave 1 pattern in relation with the Real cEOF1 (Figure 4b.1). The Imaginary cEOF1 shows a much more zonally symmetrical pattern resembling the negative SAM phase.

With the exception of the Imaginary cEOF1, it is clear that these patterns are very different than the fully zonally asymmetric versions (Fig. 2), particularly at 200 hPa. Moreover, only in the stratosphere these patterns actually show a distinguishable wave 1 pattern shifted in phase by 90º, suggesting that using the cEOF method is artificially generating a wave structure at 200hPa. Therefore, the magnitude and phase of the cEOF1 are associated with the magnitude and phase of a zonal wave only in the stratosphere. While in the troposphere, they are associated with slightly off-centre monopoles.

Figure 5 shows the regression pattern of geopotential height anomalies upon the cEOF2. Unlike for cEOF1, in this case the regression patterns are similar to the fully zonally asymmetric patterns from Figure 2. Although there are some differences (particularly in 50 hPa), the wave trains identified before are well characterised and patterns associated with the Real cEOF2 are 90º out of phase with those associated with the Imaginary cEOF2. Zonal wave
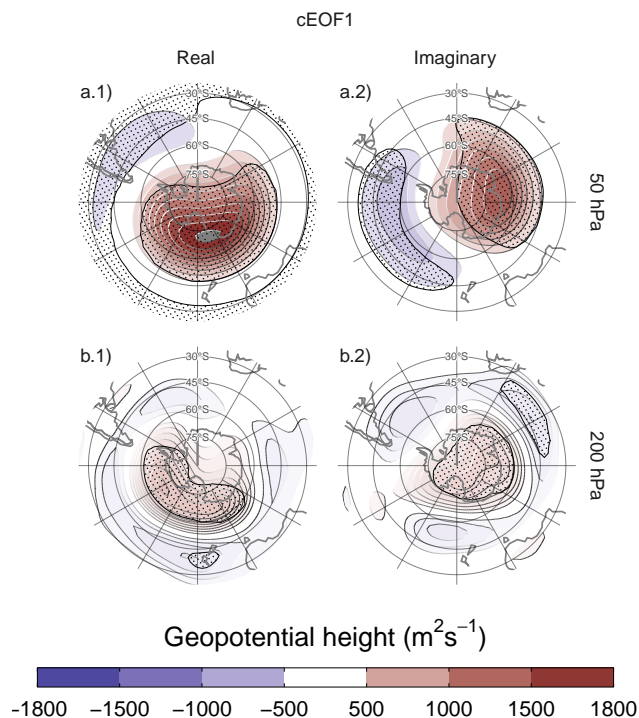
cEOF1

Real   Imaginary

a.1)   a.2)   50 hPa

b.1)   b.2)   200 hPa

Geopotential height (m^2s^{-1})

-1800 -1500 -1000 -500   500   1000   1500   1800

Fig. 4: Regression of SON geopotential height anomalies (m^2s^{-1}) with the (column 1) real and (column 2) imaginary parts of the first cEOF for the 1979 – 2019 period at (row a) 50 hPa and (row b) 200 hPa. These coefficients come from multiple linear regression involving the real and imaginary parts. Areas marked with dots have p-values smaller than 0.01 adjusted for False Detection Rate.

3 dominates all fields, but only in the western hemisphere, over the Pacific and Atlantic Oceans. cEOF2 then represents an equivalent barotropic wave train that is very similar to the the Pacific South American Patterns (Mo and Paegle 2001). Comparing the location of the positive anomaly near 90ºW in column b of Figure 5 with Figures 1.a and b from Mo and Paegle (2001), the Real cEOF2 can roughly be identified with PSA2, while the Imaginary cEOF2 resembles PSA1.

3.3 cEOFs relationship with known modes of variability

other-variables

3.3.1 SAM

sam

To explore the relationship between SAM and the modes described from the cEOF, we compute the coefficient of determination between the cEOFs time-
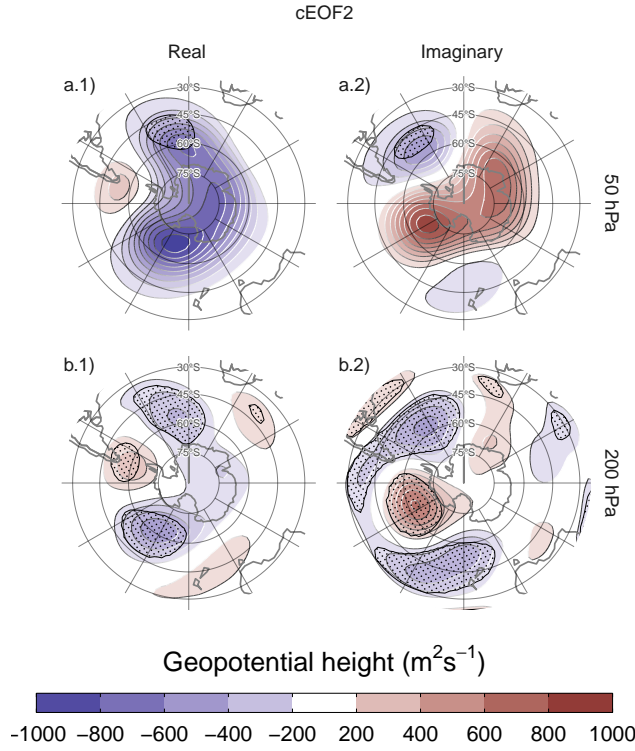
Fig. 5: Same as Figure 4 but for the second cEOF.

series and the three SAM indices (SAM, A-SAM and S-SAM) at each vertical level (Fig. 6). The SAM index is statistically signficant correlated with the Real cEOF1 in all levels, and with the Imaginary cEOF1 and Imaginary cEOF2 in the troposphere. Correlations between SAM and the Real cEOF2 are non-significant.

The relationship between the tropospheric SAM and cEOF1 is explained entirely by the zonally symmetric component of the SAM as shown by the low and statistically non-significant correlations between the A-SAM and either the Real or Imaginary cEOF1 and the high correlation with the S-SAM below 100 hPa. In the stratosphere, the Real cEOF1 is correlated with both A-SAM and S-SAM, while the Imaginary cEOF1 is highly correlated only with the A-SAM. These correlations are consistent with the regression patterns of geopotential height in Figure 4 and their comparison with those obtained for SAM, A-SAM and S-SAM by @Campitelli, Díaz, and Vera (2022).

In the case of cEOF2, the moderate correlation between SAM and Imaginary cEOF2 becomes extremely high only when the zonally asymmetric variability of the SAM is considered. The Imaginary cEOF2 explains up to 92% of A-SAM variance, reached the maximum value at 225 hPa (Figure 6.b2). Such extremely high correlation between the asymmetric SAM and the Imaginary
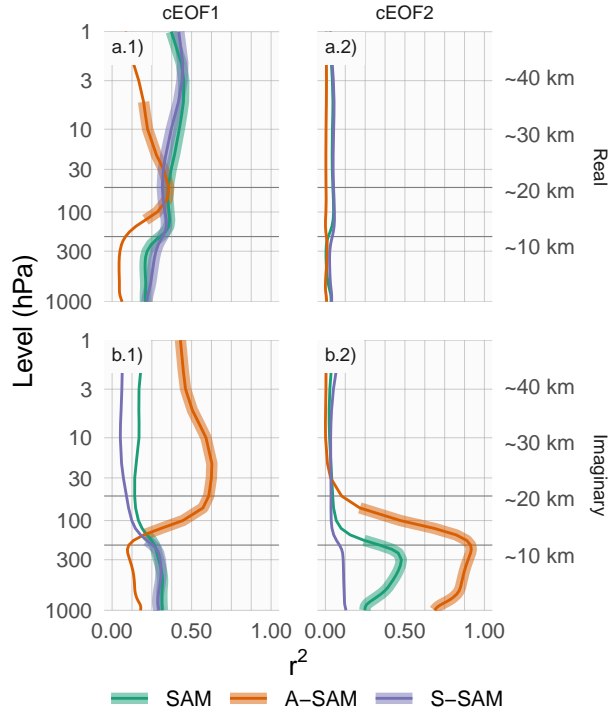
fig:sam-eof-vertical

Fig. 6: Coefficient of determination between the real and imaginary part of each cEOF and the SAM, Asymmetric SAM (A-SAM) and Symmetric SAM (S-SAM) indices computed at each level according to @Campitelli, Díaz, and Vera (2022) for the 1979 – 2019 period. Thick lines represent estimates with p-value < 0.01 corrected for False Detection Rate (Benjamini and Hochberg 1995).

cEOF2 suggests that these might be different ways of characterising the same phenomenon.

3.3.2 PSA

psa

Due to the similarity between the PSA patterns and the cEOF2 spatial patterns (Fig. 5), we study the relationship between these modes. Table 2 shows the correlations between the two PSA indices and the timeseries for Real and Imaginary phase of cEOF2. As anticipated by Figure 5, there is a strong correlation between PSA1 and Imaginary cEOF2, and between PSA2 and Real cEOF2. Conversely, there is no relationship between PSA1 and Real cEOF2, and between PSA2 and Imaginary cEOF2. As a result, cEOF2 represents well both the spatial structure and temporal evolution of the PSA modes, as well as it is possible to make a rather clean association between its two phases and the two PSA modes. So, It could be concluded that the same particular

Table 2: tab:psa-eof2 Correlations between the Real and Imaginary parts of cEOF2 and the PSA1 and PSA2 modes computed as the second and third EOFs of seasonal geopotential height anomalies (following Mo and Paegle 2001) for the 1979 – 2019 period. 95% confidence intervals in parenthesis. p-values lower than 0.01 in bold.

PC	cEOF2	
	Real	Imaginary
PSA1	0.26 (CI: -0.04 − 0.52)	**0.82 (CI: 0.69 − 0.9)**
PSA2	**0.79 (CI: 0.63 − 0.88)**	-0.02 (CI: -0.32 − 0.29)

rotation of cEOF2 that maximises the association between cEOF2 parts and PSA modes, is the one which maximises the relationship between ENSO and Imaginary cEOF2.

The reason the conventional EOF analysis arrives at the same separation than our particular cEOF rotation is probably the fact that not all phases are equally frequent. To visualize that, Figure 7 shows an histogram that counts the number of SON years in which the cEOF2 was close to each of the four particular phases (positive/negative Real/Imaginary), with the observations for each season marked as rugs on the horizontal axis. For instance, years with cEOF2 phase within 45º of 0º are nearest the "positive Real" phase. About two thirds of time cEOF2 has a phase similar to either the negative or positive Imaginary phase. It could be seen that Imaginary phase is the most common phase and It is also, by construction, the direction that has the maximum relationship with ENSO. Therefore, the Imaginary cEOF2 explains more variance than the Real cEOF2 and conventional EOF analysis will tend to separate the two.

The result obtained here is similar to the one obtained by Irving and Simmonds (2016). They show that the phase distribution of the PSA-like variability obtained by them is bimodal and isolate the PSA pattern from the rest of the PSA-like variability by selecting events that are near the peaks of the distribution (compare our Figure 7 with their Figure 6).

The advantage of our method is that it is much simpler to implement, it provides magnitude and phase naturally, and it facilitates the description of this mode as a propagating wave instead of as standing oscillations. As a consequence, the cEOF2 offers an alternative way of representing the PSA which has several advantages over using the second and third EOFs.

3.3.3 Temperature and Ozone

temperature-and-ozone

The relation between cEOFs and air temperature was also evaluated. Figure 8 shows regression patterns of air temperature at 50hPa and 200hPa onto cEOF1. In both levels, the Real cEOF1 is associated with a positive monopole over the South Pole with its centre moved slightly towards 150ºE (Fig. 8 column 1). On the other hand, the regression maps on the Imaginary cEOF1
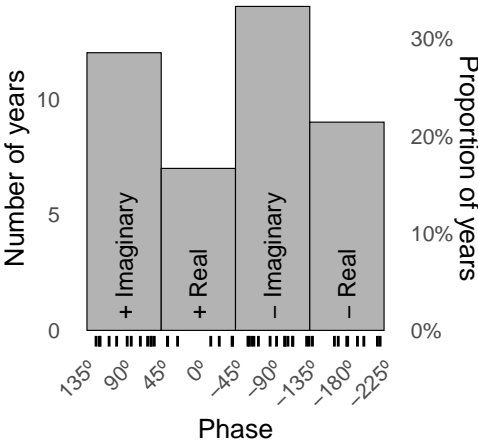
Fig. 7: Histogram of phase distribution of cEOF2 for the 1979 – 2019 period.
Bins are centred at 90º, 0º, -90º, -180º with a binwidth of 90º. The small
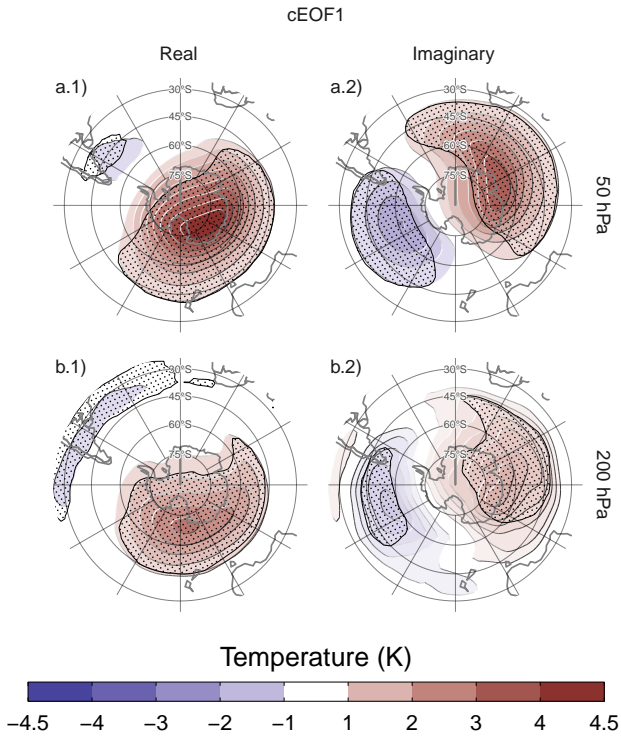vertical lines near the horizontal axis mark the observations.

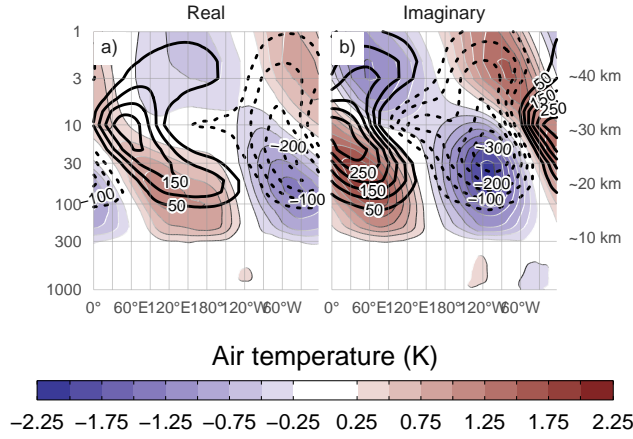Fig. 8: Same as Figure 4 but for air temperature (K).

Fig. 9: Regression of SON anomalies of mean air temperature (shaded, Kelvin) and ozone mixing ratio (contours, negative contours with dashed lines, labels in parts per billion by mass) averaged between 75°S and 45°S with the (a) real and (b) imaginary parts of the first cEOF for the 1979 – 2019 period.

show a more clear wave 1 pattern with its maximum around 60°E. The distribution of temperature regression coefficients at 50 hPa and at 200 hPa mirror the geopotential height regression maps at 50 hPa (Fig. 4).

Figure 9 shows the vertical distribution of the regression coefficients on cEOF1 from zonal anomalies of air temperature and zonal anomalies of ozone mixing ratio averaged between 75°S and 45°S. Temperature zonal anomalies associated with cEOF1 show a clear wave 1 pattern for both real and imaginary components throughout the atmosphere above 250 hPa with a change in sign above 10 hPa. Following hydrostatic balance, this is the level in which the geopotential anomaly have maximum amplitude (not shown).

The maximum ozone anomalies are co-located with the minimum temperature anomalies above 10 hPa and with the maximum temperature anomalies below 10 hPa (Fig. 9). Therefore, the ozone zonal wave 1 is anticorrelated with the temperature zonal wave 1 in the upper stratosphere, and directly correlated in the upper stratosphere. This change in phase is observed in ozone anomalies forced by planetary waves that reach the stratosphere. In the photochemically-dominated upper stratosphere, cold temperatures inhibit the destruction of ozone. On the other hand, in the advectively-dominated lower stratosphere, ozone anomalies are 90º out of phase with horizontal and vertical transport, which are in adittion 90º out of phase with temperature anomalies (Hartmann and Garcia 1979; Wirth 1993; Smith 1995).

The regression maps of cEOF1 with fields of Total Ozone Column (TOC) (Fig. 10) show zonal wave 1 pattens in TOC associated with both phases of cEOF1. Climatologically, the springtime Ozone minimum is located off the South Pole and towards the Weddell Sea (Grytsai 2011). Thus, the Real cEOF1
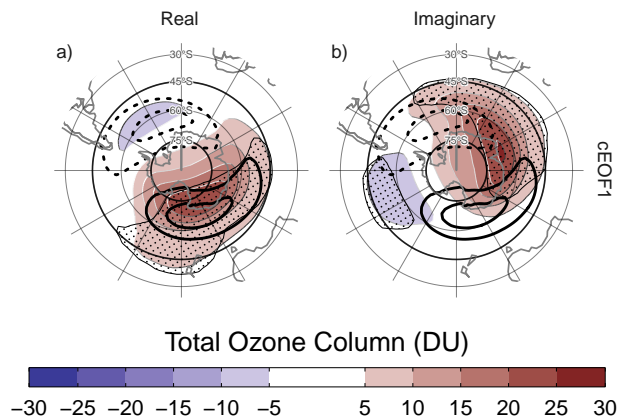
Fig. 10: fig:o3-regr Regression of SON mean Total Ozone Column anomalies (shaded, Dobson Units) with the (a) real and (b) imaginary parts of the cEOF1 for the 1979 – 2019 period. On contours, the mean zonal anomaly of Total Ozone Column (negative contours in dashed lines, Dobson Units). Areas marked with dots have p-values smaller than 0.01 adjusted for False Detection Rate.

regression pattern (Figure 10a) coincides with the climatological position of the ozone hole while the one for the Imaginary cEOF1 is shifted by 90º.

There is a close spatial relationship between amplitudes and phases of the cEOF1 and TOC planetary wave 1 between 75°S and 45°S. The correlation between the amplitude of both indices is 0.79 (CI: 0.63 – 0.88) and -0.85 (CI: -0.92 – -0.74) between their phases.

3.4 Tropical sources

tropical

The connections between cEOFs and Tropical sources are also assessed. Figure 11 shows the regression maps of Sea Surface Temperatures (SST) and streamfunction anomalies at 200 hPa respectively upon standardised cEOF2, which can be interpreted as the anomalies associated with a 1 standard deviation increase of each index. Besides showing the regression of the real and imaginary parts, we also show regressions in two intermediate directions. The Imaginary cEOF2 is associated with strong positive SST anomalies on the Central Pacific and negative anomalies over an area across the North of Australia and New Zealand, the South Pacific Convergence Zone (SPCZ) (Figure 11.b1). This pattern is almost canonically positive ENSO (Bamston, Chelliah, and Goldenberg 1997) and indeed, the correlation between the Imaginary cEOF2 and the Oceanic Niño Index (Bamston, Chelliah, and Goldenberg 1997) is significant and very high 0.76 (CI: 0.6 – 0.87). On top of this ENSO-like pattern, there are positive anomalies in the western Indian Ocean and negative values in the eastern Indian Ocean, resembling a positive Indian Ocean Dipole.
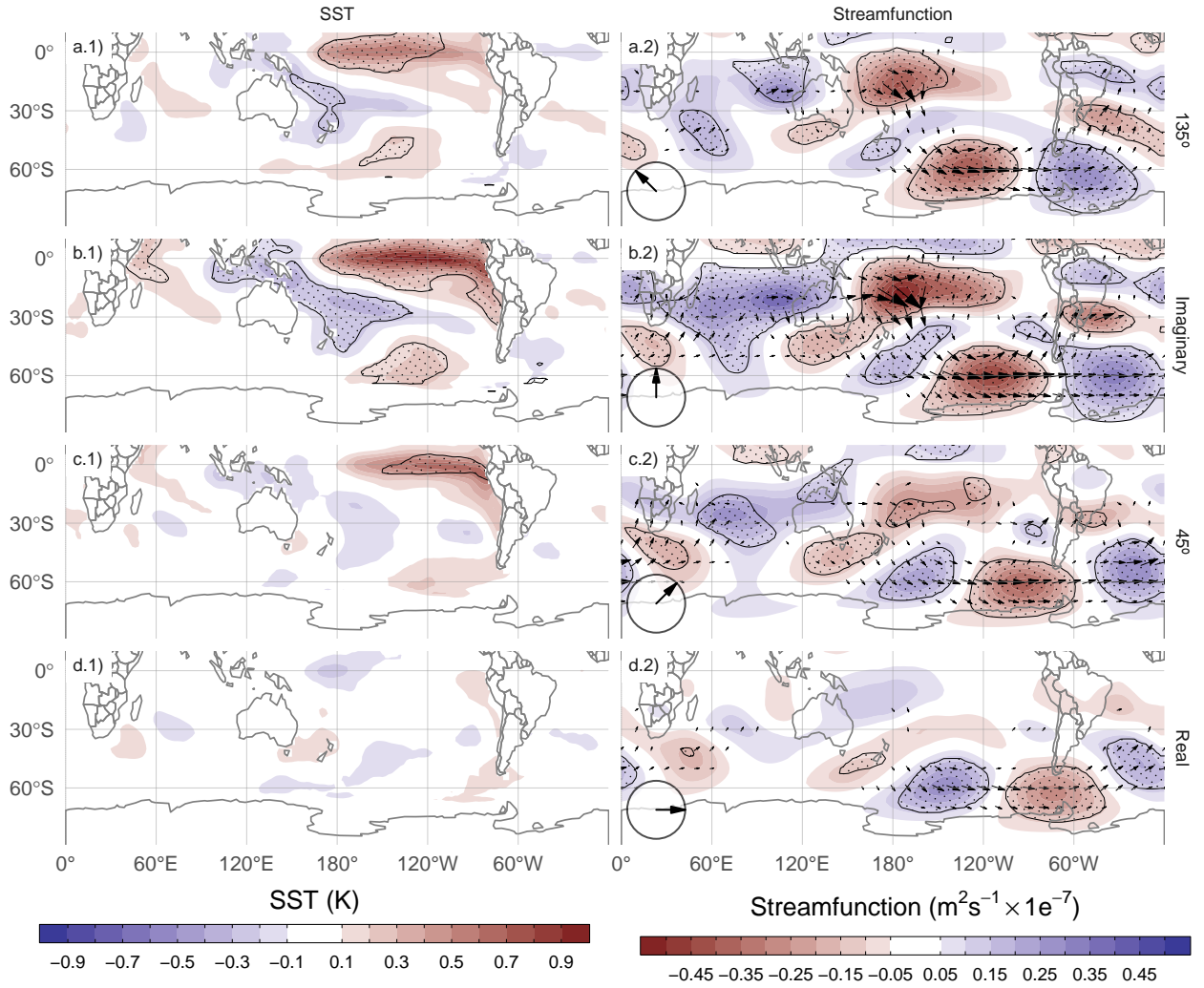
Fig. 11: Regression maps of cEOF2 with SST (K, column 1) and streamfunction zonal anomalies ($m^2/s \times 10^{-7}$, shaded) with their corresponding activity wave flux (vectors) (column 2) for the $1979 - 2019$ period and different phases of the cEOF (illustrated in the lower-left arrow). Areas marked with dots have p-values smaller than 0.01 adjusted for FDR.

`fig:sst-psi-2`

Fittingly, the Imaginary cEOF2 is also associated with strong wave-like streamfunction anomalies emanating from the tropics (Figure 11.b2), both from the Central Pacific sector and the Incean Ocean. These are consistent with the effect of ENSO and the Indian Ocean Dipole on the extratropics: the SST anomalies initiate anomalous tropical convection that excites Rossby
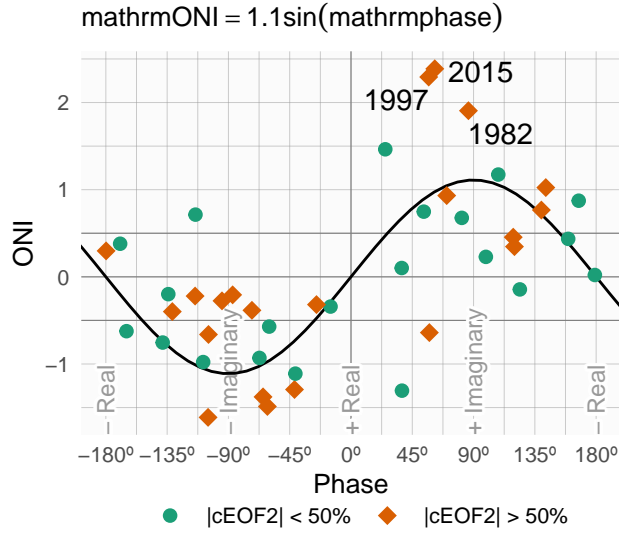
Fig. 12: ONI plotted against cEOF2 phase for th 1979 – 2019 period. Years with magnitude of cEOF2 greater or smaller than the 50th percentile are shown as orange diamonds and green circles and respectively. Black line is the fit ONI ~ sin(phase) computed by weighted OLS using the magnitude of the cEOF2 as weights.

waves that propagate meridionally towards higher latitudes (Mo 2000; Cai et al. 2011; Nuncio and Yuan 2015).

Not all phases of the cEOF2 are associated with the same tropical SSTs, however. Figure 11.d1 and d2 show that the Real cEOF2 is not associated either with any significant SST nor streamfunction anomalies in the tropics. The correlation between the Real cEOF2 and ENSO is also not significant (0 (CI: -0.3 – 0.3)). Rows a and c in Fig. 11 show that the intermediate phases are still associated with significant SST anomalies over the Pacific Ocean, but with with slightly different location. The 135º phase is associated with SST in the central Pacific, while the 45º phase is associated with SST in the eastern Pacific, which correspond roughly to the Eastern Pacific and Central Pacific "flavours" of ENSO (Citas).

To better explore the relationship between tropical forcing and phase of the cEOF2, Figure 12 shows the ONI index against the cEOF2 phase for each SON trimester between 1979 and 2019, highlighting years in which the magnitude of cEOF2 is above the median. In years with positive ONI, the phase of the cEOF2 is mostly around $+90º$ (corresponding with positive imaginary part) and vice versa. In years with near neutral ENSO, the phase of the cEOF2 is much more variable. The black line in Figure 12 is a sinusoidal fit of the relationship between ONI and cEOF2 phase. The r^2 corresponding to the fit is 0.57, statistically significant with p-value < 0.001, indicating a quasi-sinusoidal relation between these two variables.

The correlation between the absolute magnitude of the ONI and the magnitude of the cEOF2 is 0.45 (CI: 0.17 – 0.66). This relationship, however, appears to be driven only by the three years with strongest ENSO events in the period (2015, 1997, and 1982) which also coincide with the three years with strongest cEOF2 magnitude. If those years are removed, the correlation becomes non-significant (0.04 (CI: -0.28 – 0.35)). Furthermore, even when using all years, the Spearman correlation –which is robust to outliers– is also non-significant (0.2, p-value= 0.21). Therefore, although the location of tropical SST seem to have an effect in defining the phase of the cEOF2, the relationship between the magnitude of the cEOF2 train wave and ONI remains uncertain.

It could be concluded that the wave train represented by cEOF2 can be both part of the internal variability of the extratropical atmosphere or forced by tropical SSTs. In the former case, the wave train has little phase preference. However, when cEOF2 is excited by tropical SST variability, it tends to remain locked to the imaginary phase. This explains the relative over-abundance of years with cEOF2 near positive and negative imaginary phase in Figure 7.

Unlike the cEOF2 case, there is no significant pattern of SST anomalies associated with either the Real or Imaginary cEOF1 (Figure A.1). Consistently, streamfunction anomalies do not show any tropical influence. Instead, the real and Imaginary cEOF1 are associated with zonally wave activity fluxes in the extra-tropics around 60ºS, except for an equatorward flow from the coast of Antarctica around 150ºE in the real component. This suggests that its variability is driven primary by the internal variability of the extra-tropics.

3.5 Precipitation and 2-metre temperature

`precipitation`

The influence of cEOFs variability in continental rainfall and 2-metre temperature in the Southern Hemisphere is also explored. Figure 13 shows the r^2 between the cEOF1 and cEOF2 and 2-metre temperature and precipitation. For the cEOF1 there are no significant signals in precipitation and most of the temperature signal is low and restricted to the eastern coast of Antarctica.

There is a strong signal between both variables and cEOF2, with explained variance greater than 50% in some regions. For 2-metre temperature, there are high values in the tropical Pacific and the SPCZ, as well as the region following an arc between New Zealand and the South Atlantic. Over the continents, moderate values of about 30% variance explained can be seen in southern Australia, some regions of South America and the Antarctic Peninsula. For precipitation, there are high values over the tropics. At higher latitudes, moderate values are observed over eastern Australia and some regions of southern South America.

Since the cEOF1 has a relatively weak signal, we will focus on the cEOF2.

Figure 14 shows regression maps of 2-meter temperature (column 1) and precipitation (column 2) upon standardised cEOF2 which, again, can be interpreted as the anomalies associates with a 1 standard deviation increase.
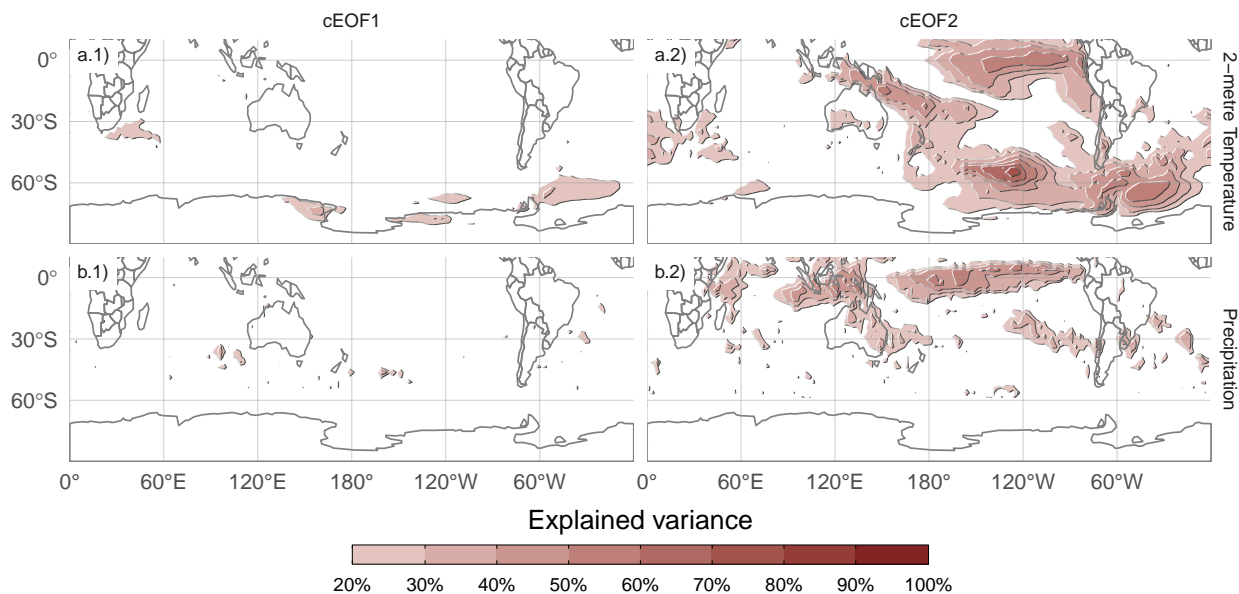
Fig. 13: fig:pp-t2m-r2 Explained variance (r^2) of 2-metre temperature (row a) and precipitation (row b) with cEOF1 (column 1) and cEOF2 (column 2).

Temperature anomalies associated with the Imaginary cEOF (Fig. 14.b1) show positive values in the tropical Pacific, consistent with SSTs anomalies associated with the same phase (Fig. 11.b1).

At higher latitudes there is a wave-like pattern of positive and negative values that coincide with the nodes of the 850hPa geopotential height regression patterns. This is consistent with temperature anomalies produced by meridional advection of temperature by the meridional winds arising from geostrophic balance.

Over the continents, the Imaginary cEOF2 (Fig. 14b.1) is associated with positive temperatures in southern Australia and negative temperature in southern South America and the Antarctic Peninsula.

The temperatures anomalies associated with the Real cEOF2 (Fig. 14d.1) are less extensive. There is no significant signal over the continents except for positive anomalies near the Antarctic Peninsula.

Tropical precipitation anomalies associated with the Imaginary cEOF2 are strong, with positive anomalies in the central Pacific and western Indian, an negative anomalies in the eastern Pacific. This pattern is consistent with the SST anomalies shown before as the increased SST enhances tropical convection and vice versa.

On the extra-tropics, the Imaginary cEOFs is correlated with drier conditions over eastern Australia; a similar signal as the one associated with ENSO Cai et al. (2011). However, the Imaginary cEOF2 is not the direction most correlated with precipitation in that area. The 135º direction (positive Imaginary
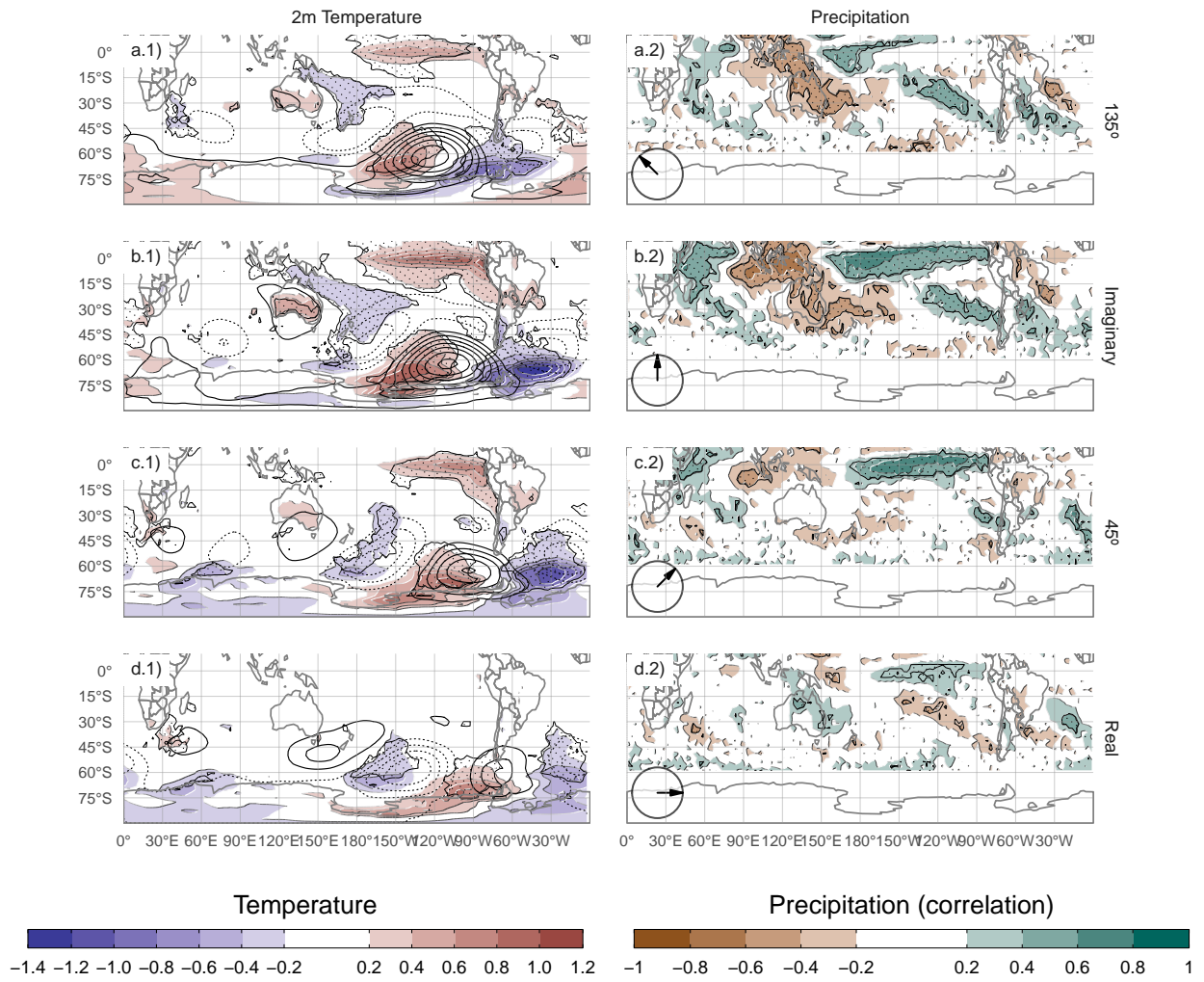
Fig. 14: Regression of SON mean 2-meter temperature (K, shaded) and 850hPa geopotential height (m, contours) (column 1), and precipitation (correlation, column 2) with different phases of cEOF2. For the 1979 – 2019. Areas marked with dots have p-values smaller than 0.01 adjusted for False Detection Rate.

+ negative Real cEOF2) is associated with stronger and more extensive correlations with precipitation over Australia and New Zealand. This Australian signal is most likely there due to the more direct impacts of ENSO rather than on the interconnection pattern represented by the cEOF2.

Over South America, the Imaginary cEOF has positive correlations with precipitation in South Eastern South America (SESA) and central Chile, and negative correlations in eastern Brazil. This again is a well-known springtime precipitation signature of ENSO (Cai et al. 2020) and it is also similar to the

precipitation anomalies associated with the A-SAM (@ Campitelli, Díaz, and Vera 2022).

This is not surprising considering the close relationship between the ONI, the A-SAM index and the Imaginary cEOF2 shown previously, but further consolidates the identification of this mode with the PSA pattern. Resembling the relationship between ONI and the phase of cEOF2 (Fig. 12), there is a cEOF2 phase dependence of the precipitation anomalies in SESA (not shown). These variables could be related with a significant sinusoidal fit that has a statistically significant coefficient of determination of 0.3.

The precipitation signal associated with the Real cEOF2 is less strong. There is a residual positive correlation in the equatorial eastern Pacific and small, not statistically significant positive correlations over eastern Australia and negative ones over New Zealand.

Lastly, the cEOF1 doesn't have a significant signal associated with 2-metre temperature or precipitacion (Fig. **??**).

4 Conclusions

conclusions

In this study we assessed the Austral Spring Extratropical Southern Hemisphere zonally assymetric circulation. For this purpose, two complex indices were derived using Complex Empirical Orthogonal Functions. This allowed us to characterise both the amplitude and phase of planetary waves that are not perfectly organised as sinusoidal waves with constant amplitude at each latitude circle.

The first complex EOF represents the variability of the zonal wave 1 in the stratosphere, but represents a more zonally symmetric monopole in the troposphere. There is a statistically positive trend in the magnitude of this cEOF, which is consistent with previous studies that showed secular changes in springtime wave-1-like patterns (e.g. M. Raphael 2003). This mode is closely related to stratospheric variability such as anomalies in Total Ozone Column. Otherwise, this complex EOF is not related with SST variability and continental precipitation in the Southern Hemisphere.

The second complex EOF represents a wave-3 pattern with maximum magnitude in the Pacific sector. Essentially, it is an alternate representation of the PSA1 and PSA2 patterns (Mo and Paegle 2001). We show that the Imaginary cEOF2 can be roughly identified with the PSA1 and the Real cEOF2 with the PSA2.

There is some disagreement in the literature of whether the phase of the PSA pattern is affected by the location of tropical SST anomalies (Irving and Simmonds 2016). We show not only that the cEOF2 tends to be in the imaginary phase (~PSA1) when the ENSO region is warm, but that central Pacific SST anomalies tend to move the cEOF towards the negative real phase and eastern Pacific SST anomalies tend to move it towards positive real phase. When ENSO is neutral, the cEOF2 is still active, but with no particular preferred phase. This mirrors the results of Cai and Watterson (2002), who showed

that the CSIRO Model can create PSA-like variability even in the absence of ENSO forcing (with a climatological run), but the variability of one of the PSA modes was enhanced when adding the ENSO signal. The magnitude of the cEOF2 appears not to be related to the magnitude of ENSO, except for the three strongest ENSO events in the period which coincide with the three strongest cEOF2 years.

The sensitivity of the phase of the cEOF2 to the location of the tropical SST anomalies was also seen by Ciasto, Simpkins, and England (2015), who detected similar Rossby wave patterns associated with central Pacific and eastern Pacific SST anomalies but with a change in phase.

We further show that the Imaginary cEOF2 is closely related to the Southern Annular Mode in the troposphere. In fact, it has a very close resemblance to the zonally asymmetric portion of the SAM. This raises the possibility that the asymmetric component of the SAM is actually a statistical contamination of the PSA mode.

Precipitation anomalies in South America associated with the Imaginary cEOF2 show a clear ENSO-like impact, with positive anomalies in South-Eastern South America, negative anomalies in Southern Brazil and positive anomalies in central Chile. Precipitation anomalies associated with the Real cEOF2 are low and not statistically significant, showing that the Imaginary phase is optimally aligned with the direction of maximum precipitation impacts.

On the other hand, over Australia, both the Real and Imaginary phase are associated with significant precipitation anomalies, and we further show that the direction of maximum impact is not aligned with our chosen rotation of cEOF2. However, this underscores the benefit of using complex EOF, since it would be trivial to rotate it. That is, look for the rotation of complex EOF that maximises the relationship and use that as the relevant index for study or forecast.

Some aspects of our work are in direct contrast with Irving and Simmonds (2016) analysis of the PSA. They didn't find neither a strong association between PSA-like variability and ENSO, nor a relationship between it and Australian precipitation. Part of the disagreement could be due to the fact that we focus data only for SON, which is when the teleconnection pattern is strongest, instead of the whole year. Irving and Simmonds (2016) use of ERA5 forectasted precipitation instead of the more observationally constrained CMAP dataset might also be an issue. But in light of the previous discussion on the importance of the phase of the cEOF2 in its relationship with ENSO and with precipitation impacts, a big difference could be fact that Irving and Simmonds (2016)'s methodology is insensitive to phase changes of the PSA-like variability.

To the extent that the cEOF2 can be identified with the PSA, what is the advantage of the technique proposed here? The spatial fields that the cEOF2 index describes are in quadrature by construction, which makes it possible to derive a proper amplitude and phase. Furthermore, because of the way they are constructed, they are not forced to be orthogonal to the SAM. This makes

it possible to study their relationship with the SAM free of the statistical contamination that comes with the usual definition of the PSA as the second and third EOFs.

Further work should extend this analysis to other seasons and further study the relationship between the cEOF2 and the SAM. In particular, it is not clear whether the close identification between the Imaginary cEOF2 and the Asymmetric SAM arises from physical processes or statistical contamination.

Code availability

`code-availability`

A version-controlled repository of the code used to create this analysis, including the code used to download the data can be found at `https://github.com/eliocamp/shceof`.
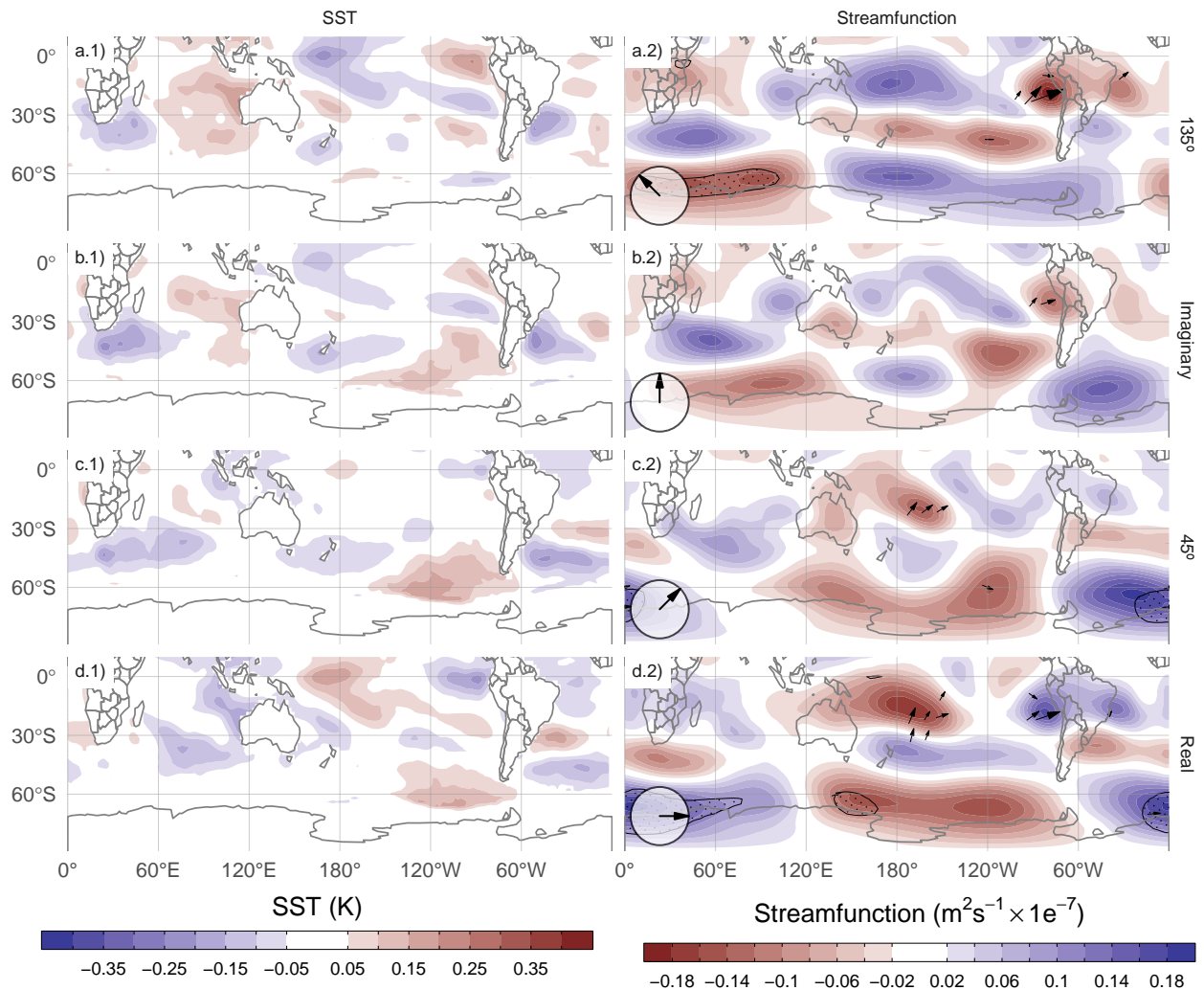
A Extra figures

`extra-figures`

Fig. A.1: Same as Figure 11 but for cEOF1. `fig:sst-psi-1`

Adams, John C., Paul N. Swartztrauber, and Roland Sweet. 1999. "FISHPACK, a Package of Fortran Subprograms for the Solution of Separable Elliptic Partial Differential Equations." 1999. https://www2.cisl.ucar.edu/resources/legacy/fishpack.

Albers, Sam, and Elio Campitelli. 2020. "Rsoi: Import Various Northern and Southern Hemisphere Climate Indices."

Allaire, J. J., Yihui Xie [aut, cre, Jonathan McPherson, Javier Luraschi, Kevin Ushey, Aron Atkins, et al. 2020. "Rmarkdown: Dynamic Documents for R."

Baldwin, Mark P., and David W. J. Thompson. 2009. "A Critical Comparison of Stratosphere–Troposphere Coupling Indices." *Quarterly Journal of the Royal Meteorological Society* 135 (644): 1661–72. https://doi.org/10.1002/qj.479.

Bamston, Anthony G., Muthuvel Chelliah, and Stanley B. Goldenberg. 1997. "Documentation of a Highly ENSO-related Sst Region in the Equatorial Pacific: Research Note." *Atmosphere-Ocean* 35 (3): 367–83. https://doi.org/10.1080/07055900.1997.9649597.
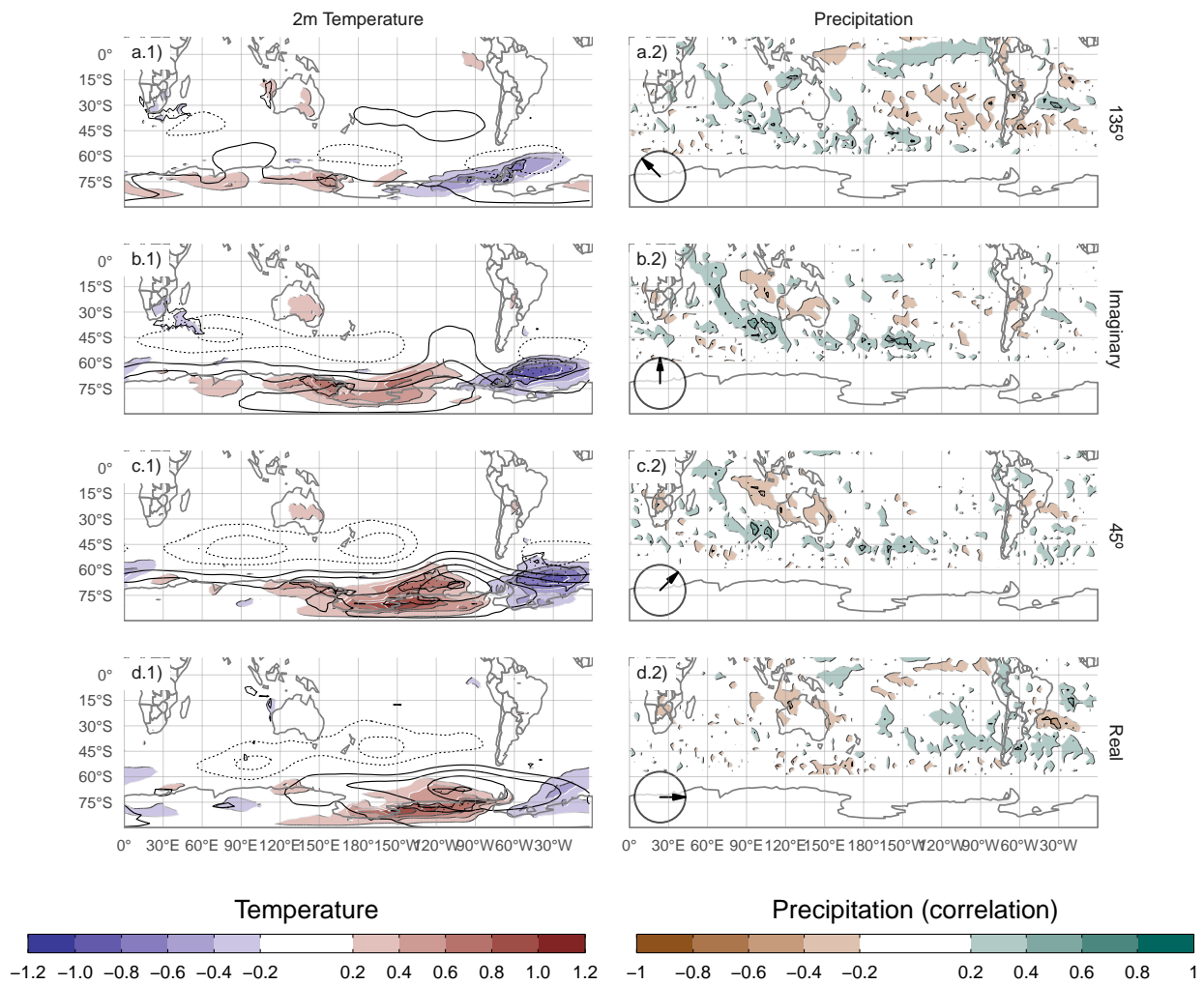
2m Temperature   Precipitation

Temperature

−1.2 −1.0 −0.8 −0.6 −0.4 −0.2   0.2 0.4 0.6 0.8 1.0 1.2

Precipitation (correlation)

−1 −0.8 −0.6 −0.4 −0.2   0.2 0.4 0.6 0.8 1

fig:pp-temp-1

Fig. A.2: Same as Figure 14 but for cEOF1.

Bell, B., H. Hersbach, P. Berrisford, P. Dahlgren, A. Horányi, J. Muñoz Sabater, J. Nicolas, et al. 2020. "Era5 Monthly Averaged Data on Pressure Levels from 1950 to 1978 (Preliminary Version)." *Copernicus Climate Change Service (C3s) Climate Data Store (CDS)* (Accessed on <26-08-2021>), https://cds.climate.copernicus.eu/cdsapp#!/dataset/reanalysis-era5-pressure-levels-monthly-means-preliminary-back-extension?tab=overview.

Benjamini, Yoav, and Yosef Hochberg. 1995. "Controlling the False Discovery Rate: A Practical and Powerful Approach to Multiple Testing." *Journal of the Royal Statistical Society: Series B (Methodological)* 57 (1): 289–300. `https://doi.org/10.1111/j.2517-6161.1995.tb02031.x`.

Cai, Wenju, Michael J. McPhaden, Alice M. Grimm, Regina R. Rodrigues, Andréa S. Taschetto, René D. Garreaud, Boris Dewitte, et al. 2020. "Climate Impacts of the El Niño–Southern Oscillation on South America." *Nature Reviews Earth & Environment* 1 (4, 4): 215–31. `https://doi.org/10.1038/s43017-020-0040-3`.

Cai, Wenju, Peter van Rensch, Tim Cowan, and Harry H. Hendon. 2011. "Teleconnection Pathways of ENSO and the IOD and the Mechanisms for Impacts on Australian Rainfall." *Journal of Climate* 24 (15): 3910–23. `https://doi.org/10.1175/2011JCLI4129.1`.

Cai, Wenju, and Ian G. Watterson. 2002. "Modes of Interannual Variability of the Southern Hemisphere Circulation Simulated by the CSIRO Climate Model." *Journal of Climate* 15 (10): 1159–74. `https://doi.org/10.1175/1520-0442(2002)015%3C1159:MOIVOT%3E2.0.CO;2`.

Campitelli, Elio. 2020. "metR: Tools for Easier Analysis of Meteorological Fields."

Campitelli, Elio, Leandro B. Díaz, and Carolina Vera. 2022. "Assessment of Zonally Symmetric and Asymmetric Components of the Southern Annular Mode Using a Novel Approach." *Climate Dynamics* 58 (1): 161–78. `https://doi.org/10.1007/s00382-021-05896-5`.

Cazes-Boezio, Gabriel, Andrew W. Robertson, and Carlos R. Mechoso. 2003. "Seasonal Dependence of ENSO Teleconnections over South America and Relationships with Precipitation in Uruguay." *Journal of Climate* 16 (8): 1159–76. `https://doi.org/10.1175/1520-0442(2003)16%3C1159:SDOETO%3E2.0.CO;2`.

Ciasto, Laura M., Graham R. Simpkins, and Matthew H. England. 2015. "Teleconnections Between Tropical Pacific SST Anomalies and Extratropical Southern Hemisphere Climate." *Journal of Climate* 28 (1): 56–65. `https://doi.org/10.1175/JCLI-D-14-00438.1`.

Dowle, Matt, and Arun Srinivasan. 2020. "Data.table: Extension of 'Data.frame'."

Fogt, Ryan L., and Gareth J. Marshall. 2020. "The Southern Annular Mode: Variability, Trends, and Climate Impacts Across the Southern Hemisphere." *WIREs Climate Change* 11 (4): e652. `https://doi.org/10.1002/wcc.652`.

Gelbrecht, Maximilian, Niklas Boers, and Jürgen Kurths. 2018. "Phase Coherence Between Precipitation in South America and Rossby Waves." *Science Advances* 4 (12): eaau3191. `https://doi.org/10.1126/sciadv.aau3191`.

Gong, Daoyi, and Shaowu Wang. 1999. "Definition of Antarctic Oscillation Index." *Geophysical Research Letters* 26 (4): 459–62. `https://doi.org/10.1029/1999GL900003`.

Grytsai, A. 2011. "Planetary Wave Peculiarities in Antarctic Ozone Distribution During 1979–2008." *International Journal of Remote Sensing* 32 (11): 3139–51. `https://doi.org/10.1080/01431161.2010.541518`.

Hartmann, Dennis L., and Rolando R. Garcia. 1979. "A Mechanistic Model of Ozone Transport by Planetary Waves in the Stratosphere." *Journal of the Atmospheric Sciences* 36 (2): 350–64. `https://doi.org/10.1175/1520-0469(1979)036%3C0350:AMMOOT%3E2.0.CO;2`.

Hersbach, H., B. Bell, P. Berrisford, G. Biavati, A. Horányi, J. Muñoz Sabater, J. Nicolas, et al. 2019. "Era5 Monthly Averaged Data on Pressure Levels from 1979 to Present." *Copernicus Climate Change Service (C3s) Climate Data Store (CDS)* (Accessed on <07-09-2021>). `https://doi.org/10.24381/cds.6860a573`.

Hobbs, William R., and Marilyn N. Raphael. 2010. "Characterizing the Zonally Asymmetric Component of the SH Circulation." *Climate Dynamics* 35 (5): 859–73. `https://doi.org/10.1007/s00382-009-0663-z`.

Horel, J. D. 1984. "Complex Principal Component Analysis: Theory and Examples." *Journal of Applied Meteorology and Climatology* 23 (12): 1660–73. `https://doi.org/10.1175/1520-0450(1984)023%3C1660:CPCATA%3E2.0.CO;2`.

Hoskins, B. J., and K. I. Hodges. 2005. "A New Perspective on Southern Hemisphere Storm Tracks." *Journal of Climate* 18 (20): 4108–29. `https://doi.org/10.1175/JCLI3570.1`.

Huang, Boyin, Peter W. Thorne, Viva F. Banzon, Tim Boyer, Gennady Chepurin, Jay H. Lawrimore, Matthew J. Menne, Thomas M. Smith, Russell S. Vose, and Huai-Min Zhang. 2017. "Extended Reconstructed Sea Surface Temperature, Version 5 (ERSSTv5): Upgrades, Validations, and Intercomparisons." *Journal of Climate* 30 (20): 8179–8205. `https://doi.org/10.1175/JCLI-D-16-0836.1`.

Hufkens, Koen. 2020. "Ecmwfr: Programmatic Interface to the Two European Centre for Medium-Range Weather Forecasts API Services."

Irving, Damien, and Ian Simmonds. 2015. "A Novel Approach to Diagnosing Southern Hemisphere Planetary Wave Activity and Its Influence on Regional Climate Variability." *Journal of Climate* 28 (23): 9041–57. `https://doi.org/10.1175/JCLI-D-15-0287.1`.

———. 2016. "A New Method for Identifying the Pacific–South American Pattern and Its Influence on Regional Climate Variability." *Journal of Climate* 29 (17): 6109–25. https://doi.org/10.1175/JCLI-D-15-0843.1.

Katz, Richard W., and Barbara G. Brown. 1991. "The Problem of Multiplicity in Research on Teleconnections." *International Journal of Climatology* 11 (5): 505–13. https://doi.org/10.1002/joc.3370110504.

Krokhin, V. V., and W. M. J. Luxemburg. 2007. "Temperatures and Precipitation Totals over the Russian Far East and Eastern Siberia: Long-Term Variability and Its Links to Teleconnection Indices." *Hydrology and Earth System Sciences* 11 (6): 1831–41. https://doi.org/10.5194/hess-11-1831-2007.

Laurel-Castillo, J. A., and A. Valle-Levinson. 2020. "Tidal and Subtidal Variations in Water Level Produced by Ocean-River Interactions in a Subtropical Estuary." *Journal of Geophysical Research: Oceans* 125 (7): e2018JC014116. https://doi.org/10.1029/2018JC014116.

Lim, E.-P., H. H. Hendon, and D. W. J. Thompson. 2018. "Seasonal Evolution of Stratosphere-Troposphere Coupling in the Southern Hemisphere and Implications for the Predictability of Surface Climate." *Journal of Geophysical Research: Atmospheres* 123 (21): 12, 002–12, 016. https://doi.org/10.1029/2018JD029321.

Loon, Harry van, and Roy L. Jenne. 1972. "The Zonal Harmonic Standing Waves in the Southern Hemisphere." *Journal of Geophysical Research* 77 (6): 992–1003. https://doi.org/10.1029/JC077i006p00992.

Mo, Kingtse C. 2000. "Relationships Between Low-Frequency Variability in the Southern Hemisphere and Sea Surface Temperature Anomalies." *Journal of Climate* 13 (20): 3599–3610. https://doi.org/10.1175/1520-0442(2000)013%3C3599:RBLFVI%3E2.0.CO;2.

Mo, Kingtse C., and Julia N. Paegle. 2001. "The Pacific–South American Modes and Their Downstream Effects." *International Journal of Climatology* 21 (10): 1211–29. https://doi.org/10.1002/joc.685.

Nuncio, M., and Xiaojun Yuan. 2015. "The Influence of the Indian Ocean Dipole on Antarctic Sea Ice*." *Journal of Climate* 28 (7): 2682–90. https://doi.org/10.1175/JCLI-D-14-00390.1.

Pezza, Alexandre Bernardes, Harun A. Rashid, and Ian Simmonds. 2012. "Climate Links and Recent Extremes in Antarctic Sea Ice, High-Latitude Cyclones, Southern Annular Mode and ENSO." *Climate Dynamics* 38 (1): 57–73. https://doi.org/10.1007/s00382-011-1044-y.

Plumb, R. Alan. 1985. "On the Three-Dimensional Propagation of Stationary Waves." *Journal of the Atmospheric Sciences* 42 (3): 217–29. https://doi.org/10.1175/1520-0469(1985)042%3C0217:OTTDPO%3E2.0.CO;2.

R Core Team. 2020. *R: A Language and Environment for Statistical Computing*. Manual. Vienna, Austria: R Foundation for Statistical Computing.

Raphael, M. N. 2004. "A Zonal Wave 3 Index for the Southern Hemisphere." *Geophysical Research Letters* 31 (23). https://doi.org/10.1029/2004GL020365.

———. 2007. "The Influence of Atmospheric Zonal Wave Three on Antarctic Sea Ice Variability." *Journal of Geophysical Research: Atmospheres* 112 (D12). https://doi.org/10.1029/2006JD007852.

Raphael, Marilyn. 2003. "Recent, Large-Scale Changes in the Extratropical Southern Hemisphere Atmospheric Circulation." *Journal of Climate* 16 (17): 2915–24. https://doi.org/10.1175/1520-0442(2003)016%3C2915:RLCITE%3E2.0.CO;2.

Smith, Anne K. 1995. "Numerical Simulation of Global Variations of Temperature, Ozone, and Trace Species in the Stratosphere." *Journal of Geophysical Research: Atmospheres* 100 (D1): 1253–69. https://doi.org/10.1029/94JD02395.

Trenberth, Kevin E. 1980. "Planetary Waves at 500 Mb in the Southern Hemisphere." *Monthly Weather Review* 108 (9): 1378–89. https://doi.org/10.1175/1520-0493(1980)108%3C1378:PWAMIT%3E2.0.CO;2.

Trenberth, Kevin F., and K. C. Mo. 1985. "Blocking in the Southern Hemisphere." *Monthly Weather Review* 113 (1): 3–21. https://doi.org/10.1175/1520-0493(1985)113%3C0003:BITSH%3E2.0.CO;2.

Turner, John, J. Scott Hosking, Thomas J. Bracegirdle, Tony Phillips, and Gareth J. Marshall. 2017. "Variability and Trends in the Southern Hemisphere High Latitude, Quasi-

Stationary Planetary Waves." *International Journal of Climatology* 37 (5): 2325–36. https://doi.org/10.1002/joc.4848.

Walker, Sir Gilbert Thomas. 1914. *Correlation in Seasonal Variations of Weather, III: On the Criterion for the Reality of Relationships Or Periodicities*. Meteorological Office. https://books.google.com?id=cuGtuAAACAAJ.

Wickham, Hadley. 2009. *Ggplot2: Elegant Graphics for Data Analysis*. Use R! New York: Springer-Verlag. https://doi.org/10.1007/978-0-387-98141-3.

Wilks, D. S. 2016. "'The Stippling Shows Statistically Significant Grid Points': How Research Results Are Routinely Overstated and Overinterpreted, and What to Do about It." *Bulletin of the American Meteorological Society* 97 (12): 2263–73. https://doi.org/10.1175/BAMS-D-15-00267.1.

Wilks, Daniel. 2011. *Statistical Methods in the Atmospheric Sciences*. Vol. 100. Elsevier. https://doi.org/10.1016/B978-0-12-385022-5.00022-1.

Wirth, Volkmar. 1993. "Quasi-Stationary Planetary Waves in Total Ozone and Their Correlation with Lower Stratospheric Temperature." *Journal of Geophysical Research: Atmospheres* 98 (D5): 8873–82. https://doi.org/10.1029/92JD02820.

Xie, Pingping, and Phillip A. Arkin. 1997. "Global Precipitation: A 17-Year Monthly Analysis Based on Gauge Observations, Satellite Estimates, and Numerical Model Outputs." *Bull. Amer. Meteor. Soc.* 78 (Accessed on <26-08-2021>) (11): 2539–58. https://doi.org/10.1175/1520-0477(1997)078%3C2539:GPAYMA%3E2.0.CO;2.

Xie, Yihui. 2015. *Dynamic Documents with R and Knitr*. Second. Boca Raton, Florida: Chapman and Hall/CRC.